NANO LETTERS

pubs.acs.org/NanoLett Letter

All-Electrical Spin-to-Charge Conversion in Sputtered Bi_xSe_{1-x}

Won Young Choi,* Isabel C. Arango, Van Tuong Pham, Diogo C. Vaz, Haozhe Yang, Inge Groen, Chia-Ching Lin, Emily S. Kabir, Kaan Oguz, Punyashloka Debashis, John J. Plombon, Hai Li, Dmitri E. Nikonov, Andrey Chuvilin, Luis E. Hueso, Ian A. Young, and Fèlix Casanova*

Cite This: *Nano Lett.* 2022, 22, 7992−7999 Read Online

ACCESS | Metrics & More | Article Recommendations | Supporting Information

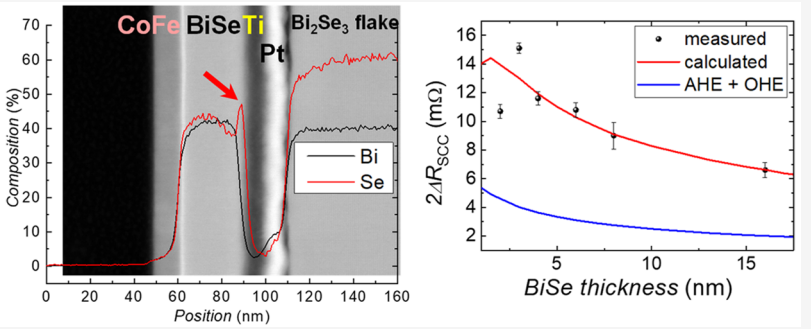

ABSTRACT: One of the major obstacles to realizing spintronic devices such as MESO logic devices is the small signal magnitude used for magnetization readout, making it important to find materials with high spin-to-charge conversion efficiency. Although intermixing at the junction of two materials is a widely occurring phenomenon, its influence on material characterization and the estimation of spin-to-charge conversion efficiencies are easily neglected or underestimated. Here, we demonstrate all-electrical spin-to-charge conversion in Bi_xSe_{1-x} nanodevices and show how the conversion efficiency can be overestimated by tens of times depending on the adjacent metal used as a contact. We attribute this to the intermixing-induced compositional change and the properties of a polycrystal that lead to drastic changes in resistivity and spin Hall angle. Strategies to improve the spin-to-charge conversion signal in similar structures for functional devices are discussed.

KEYWORDS: *MESO logic device, spin-to-charge conversion, sputtered BiSe, intermixing*

The improvement of computational performance over the past few decades has relied on an increase in the number of transistors led by the successful miniaturization of complementary metal−oxide−semiconductor (CMOS) transistors.[1] However, further improvement in performance is limited by unscaled power density,[2,3] triggering an increasing demand for energy-efficient beyond-CMOS devices that address this problem. The magnetoelectric spin−orbit (MESO) logic device[4−6] proposed in 2018 as an alternative to a CMOS device operates at very low power because it uses a magnetoelectric material for magnetization switching (writing). On the other hand, the reading part of the device[7] includes a spin−orbit material that requires a high output voltage of 100 mV[4−6] for full operation. In order to obtain such a large output voltage through spin-to-charge conversion (SCC), both high resistivity and high conversion efficiency are required.

Topological insulators (TIs) are a new class of materials[8,9] that have topologically protected surface states with spin-momentum locking, a property that should lead to very efficient SCC.[10] Indeed, TIs are considered to have an exceptionally large spin Hall angle, θ_{SH}, according to spin−orbit torque results,[11−15] and a long inverse Rashba−Edelstein length, λ_{IREE}, in a proximitized TI/graphene system.[16] Together with high resistivity, as bulk conduction is limited,[17,18] they satisfy the required conditions for MESO. Simultaneously, they have limitations in stoichiometric and single-crystalline material growth and require a low operating temperature for electrical spin injection.[19,20] Unlike epitaxially grown TIs, sputtered Bi_xSe_{1-x} was reported to have high conversion efficiency and resistivity even at room temperature, despite its simple growth technique and polycrystalline structure.[21] However, recent reports on the formation of an interfacial layer between Bi_2Se_3 and transition metals by a solid-state reaction[22−25] encourages a rigorous characterization of sputtered Bi_xSe_{1-x}.

Received: August 30, 2022
Revised: September 21, 2022
Published: September 26, 2022

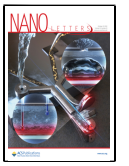

https://doi.org/10.1021/acs.nanolett.2c03429
Nano Lett. 2022, 22, 7992−7999

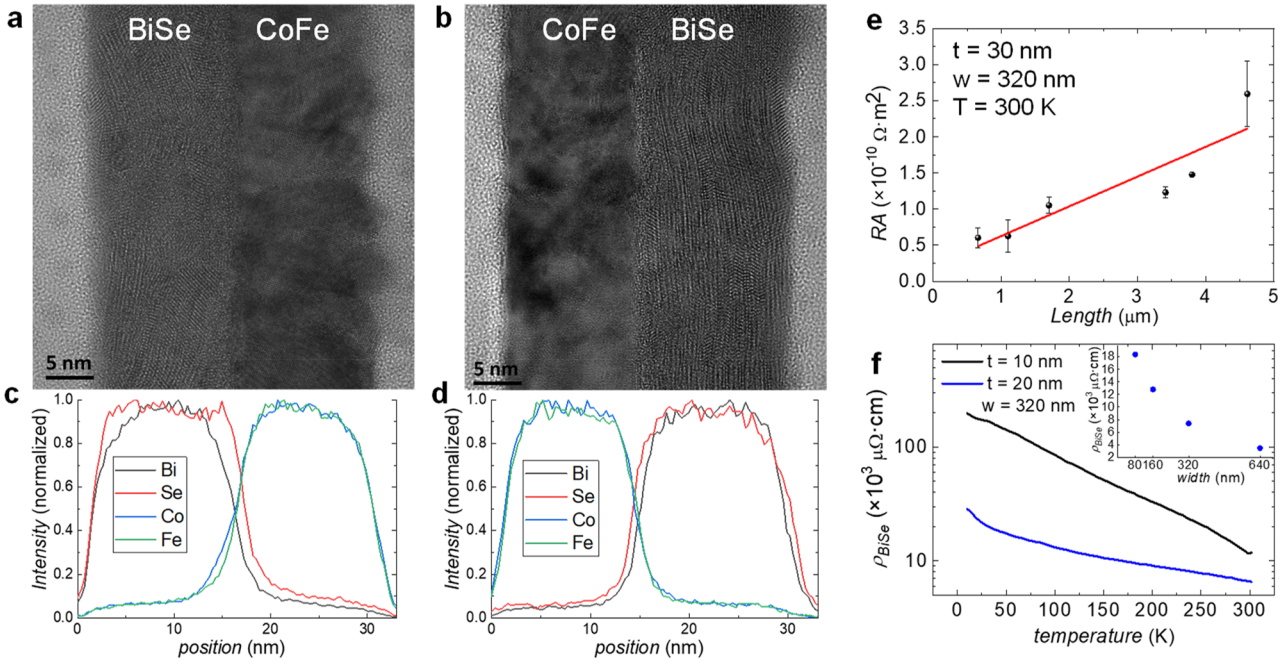

Figure 1. Characterization of sputtered BiSe. (a–d) TEM images and normalized EDX results of BiSe/CoFe (a, c) and CoFe/BiSe (b, d) bilayer stacks. (e) Length dependence of the resistance area product measured for a 320-nm-wide and 30-nm-thick wire at room temperature. From the linear fitting, a resistivity of 4000 $\mu\Omega$ cm is determined. (f) Resistivity of BiSe as a function of temperature for 320-nm wide wires with thicknesses of 10 nm (black) and 20 nm (blue). Inset: width dependence of the resistivity of a 20-nm-thick BiSe wire.

Here, we show the influence of the intermixing at the junction of Bi_xSe_{1-x} (from now on, BiSe) and transition metals on the characterization of the electrical and spintronic properties of BiSe using a local spin injection device. Sputtered BiSe was characterized by transmission electron microscopy (TEM), energy-dispersive X-ray spectroscopy (EDX), electrical measurements, and 3D finite element method (FEM) simulations. We observed a huge variation in resistivity and θ_{SH}, according to the compositional change of BiSe due to the adjacent metal layer, through the BiSe thickness dependence of the spin-to-charge conversion signal and the cross-junction resistance. This result emphasizes the importance of proper material characterization, as it can greatly affect the SCC efficiency evaluation, particularly in the case of structures or devices including reactive materials such as BiSe and transition metals.

Thin-film bilayers composed of BiSe (16 nm thick) and CoFe (15 nm thick) were prepared to characterize sputtered BiSe prior to SCC experiments. TEM images in Figure 1a,b show the structures of the SiO_2 substrate/BiSe/CoFe/capping layer and SiO_2 substrate/CoFe/BiSe/capping layer, respectively. The sputtered BiSe layer is polycrystalline in both cases, in agreement with the literature,[21] although it is more oriented on top of the CoFe layer than on top of the SiO_2 substrate. In both cases, an amorphous layer was found at the interface, being thicker in the BiSe/CoFe stack. Such a layer corresponds to intermixing at the interface, as confirmed by normalized EDX, which shows a clear shift of the Se curve (red) in both cases, as shown in Figure 1c,d, being larger in the BiSe/CoFe stack in agreement with the thicker amorphous layer. Since such an imperfection at the interface will adversely affect the spin injection between the two materials and the subsequent SCC, we chose the CoFe/BiSe stack (Figure 1b,d).

The high resistivity of sputtered BiSe is one of the reasons it is considered the strongest candidate for the magnetic readout part of MESO logic devices.[4−6] Figure 1e shows the resistance area product of a 30-nm-thick and 320-nm-wide BiSe wire measured at room temperature at different distances using metallic contacts. The resistivity of the BiSe nanowire (4000 ± 1000 $\mu\Omega$ cm) was obtained from a linear fitting (Note S1 in the Supporting Information). Unlike metallic conductors, BiSe has a high noise level in electrical measurements and a large dispersion from the fitting line. As shown in Figure 1f, the resistivity increases as the temperature decreases, indicating a semiconducting behavior, and varies with the thickness (10 and 20 nm) and width (80−640 nm). The BiSe wire with 80 nm width and 20 nm thickness has a resistivity of 18000 $\mu\Omega$ cm at room temperature, which shows that the sputtered BiSe used in this experiment is similar to those previously reported.[21]

To study SCC in BiSe, we use a local spin injection device, which corresponds to the architecture of the spin−orbit reading module of the MESO device. All materials constituting the local spin injection device were grown by dc (metallic layers) and rf (BiSe and SiO_2 capping layers) sputter deposition. The device consists of a top T-shaped nanostructure of BiSe (2−40 nm)/NM (Ti, Pt, or Ta; 10 nm) and a bottom 15-nm-thick CoFe electrode, all with a width of 80 nm. Since sputtered BiSe has a high noise level in electrical measurements, a normal metal (NM) such as Ti, Pt, or Ta is deposited on top of BiSe to pick up the SCC output voltage through electrical shunting. All measurements presented below were obtained at room temperature. Fabrication steps, characterization techniques, and measurement details are described in Methods.

To quantify the SCC signal, the transverse voltage (V_T) is measured while an external magnetic field is applied along the easy axis of the CoFe electrode (x axis) and a current (I_C) flows from CoFe to one end of the BiSe/NM T-shaped nanostructure, as shown in Figure 2a. The reciprocal

https://doi.org/10.1021/acs.nanolett.2c03429
Nano Lett. 2022, 22, 7992−7999

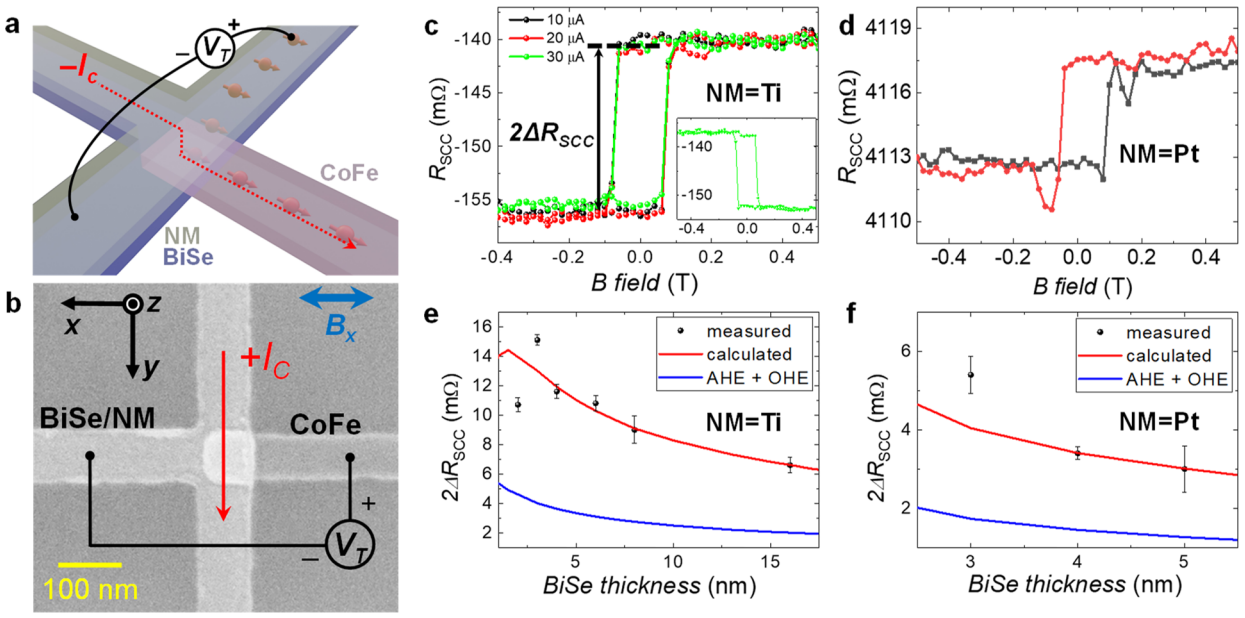

Figure 2. Local spin injection device and SCC signals. (a) Schematic of the local spin injection device and SCC measurement configuration. A vertical spin current at the junction produces a charge current in the transverse direction. (b) SEM image of the device with a measurement geometry of charge-to-spin conversion. (c, d) SCC resistance (R_{SCC}) measured using the configuration in (a) as a function of magnetic field along the x axis of (c) BiSe (3 nm)/Ti (10 nm) and (d) BiSe (3 nm)/Pt (10 nm) structures. Inset: charge-to-spin conversion resistance measured using the configuration in (b) as a function of the magnetic field along the x axis. (e, f) The SCC signal ($2\Delta R_{SCC}$) as a function of BiSe thickness and fitting curves obtained by 3D FEM simulations of (e) BiSe/Ti and (f) BiSe/Pt structures. All measurements were performed at room temperature.

measurement (charge-to-spin conversion, CSC) is described in Figure 2b. Spin-polarized current in the CoFe wire flows vertically through BiSe to the NM due to the large difference in resistivity, and SCC occurs inside BiSe. The resulting charge current is then measured transversely in the T-shaped structure as an open circuit voltage V_T. When the magnetization of the CoFe electrode is switched, the spin polarization also reverses and V_T changes sign. The SCC resistance, defined as $R_{SCC} = V_T/I_C$, always contains a baseline value, and therefore it is more convenient to define the SCC signal, $2\Delta R_{SCC}$, as the difference between the two magnetic states (see Figure 2c). The converted current is mostly shunted by CoFe and, since the NM completely covers the BiSe T-shaped nanostructure, partially by the NM greatly reducing the magnitude of V_T. What we finally measure is the voltage across the Hall cross shunted by the NM, thus being dependent on the resistivity of the NM. Nevertheless, the use of a NM layer is crucial, as it dramatically lowers the noise level and makes the SCC signal measurable, in contrast to the use of lateral NM contacts in a BiSe-only T-shaped nanostructure.

Figure 2c shows the SCC signal of 15.1 ± 0.4 mΩ measured on a BiSe (3 nm)/Ti (10 nm) device. The hysteresis loop was observed according to the switching field of the CoFe wire, and the current dependence and reciprocal measurement (CSC signal shown in the inset of Figure 2c) confirm that they were conducted in the linear response regime, which rules out the presence of any heating-related effects. The same measurement on a BiSe (3 nm)/Pt (10 nm) device is shown in Figure 2d, with an SCC signal of 5.4 ± 0.5 mΩ, which is 3 times smaller than that of a BiSe/Ti device with the same thickness.

Since the spin Hall effect can occur in the adjacent NM when BiSe is thin, we need to check whether the SCC signal is generated in BiSe. On comparison of the SCC signals of the two devices, however, θ_{SH} of Ti is negligible (−0.00036)[26] while Pt is known as a material which has high θ_{SH} (~0.1),[27,28] so even considering the high resistivity of Ti, the larger SCC signal observed cannot be properly explained. As a further check, we also fabricated devices with Ta as the NM. The sign of θ_{SH} in Ta is opposite to that of Pt, but the SCC signal of a BiSe (2 nm)/Ta (10 nm) device has the same sign as those of the other devices (Note S2 in the Supporting Information), clearly showing that the SCC appears in the thin BiSe layer, regardless of the NM used.

Figure 2e shows $2\Delta R_{SCC}$ as a function of the BiSe thickness in the BiSe (2−16 nm)/Ti (10 nm) local spin injection devices. $2\Delta R_{SCC}$ is the largest for 3 nm of BiSe, and it decreases for thicker structures. The same experiment was conducted with BiSe (3−5 nm)/Pt (10 nm), as shown in Figure 2f, yielding a similar trend. The SCC signal could only be observed up to 16 nm of BiSe for Ti and up to 5 nm for Pt, with no signal obtained at a thickness beyond that, mostly due to the increasingly higher noise level and low SCC signal.

We should mention that an anomalous Hall effect (AHE)[7,29,30] and ordinary Hall effect (OHE)[31] can appear as artifacts in the measured SCC signals (Note S3 in the Supporting Information). The anomalous Hall angle obtained by applying an out-of-plane magnetic field to CoFe in our own devices is 1.5%. In the local spin injection device, the contribution of the AHE is greatly reduced, since the magnetization points along the x axis and only the contribution by the current flowing in the z axis is considered. The contribution of the AHE was calculated by a 3D finite element method (FEM) based on the spin diffusion model,[7,29,30,32] and we obtained less than 6 and 2 mΩ AHE signals in the whole thickness range for BiSe/Ti and BiSe/Pt structures, respectively. Additionally, the stray field of CoFe-induced OHE is calculated by 3D FEM simulation based on the Hall coefficient of BiSe/NM structures obtained by applying the out-of-plane magnetic field to each structure.[31] We obtained less than a 0.3 mΩ OHE contribution for both structures. As shown in Figure

https://doi.org/10.1021/acs.nanolett.2c03429
Nano Lett. 2022, 22, 7992−7999

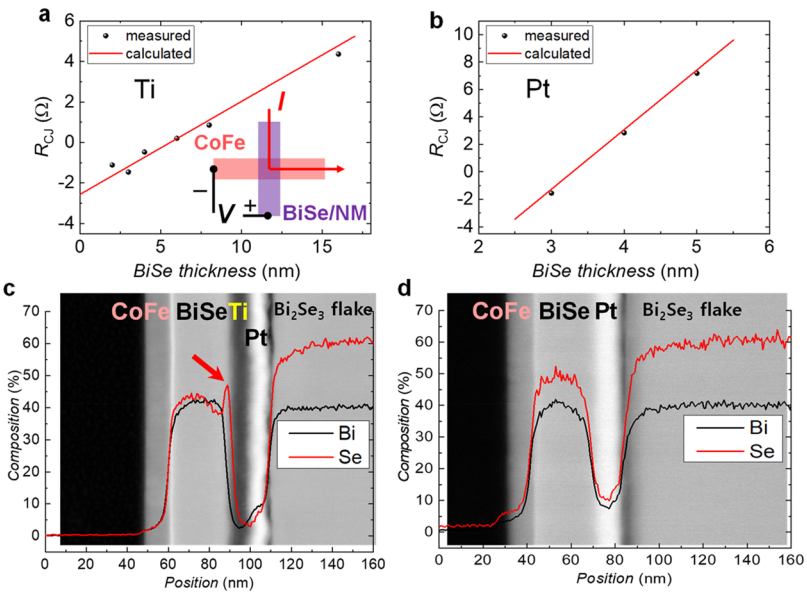

Figure 3. Estimation of BiSe resistivity in the vertical direction. Cross-junction resistances of (a) BiSe/Ti and (b) BiSe/Pt structures. Inset in (a): measurement geometry. TEM images and EDX scans of (c) CoFe/BiSe/Ti and (d) CoFe/BiSe/Pt thin-film structures compared with single-crystal Bi_2Se_3 flakes exfoliated on top for a proper quantification of the composition of the sputtered BiSe layers.

2e,f, the calculated AHE and OHE signals decay with BiSe thickness, since current shunting is suppressed and the distance between FM and NM increases, respectively.

Next, we analyzed the thickness dependence of the SCC signal by a 3D FEM simulation[7] also taking into account the AHE and the OHE discussed above (see Note S4 in the Supporting Information for details). The simulation is performed by assuming that the resistivity of BiSe is 18000 $\mu\Omega$ cm (20-nm-thick and 80-nm-wide wire in Figure 1d). The resistivities of CoFe and Ti were 42 and 40 $\mu\Omega$ cm, respectively, which were measured directly on the device. The obtained spin diffusion length (λ_s) is 0.5 nm and θ_{SH} is 27.5 (see Figure S4d), a very large value that is in a good agreement with the previously reported value, 18.62,[21] and it seems to prove once again that sputtered BiSe is one of the most promising materials for SCC devices, in particular for the MESO logic device, which also requires a high resistivity.

However, unlike the previous report, the quantum confinement[21] cannot be confirmed here, as a single θ_{SH} value of 27.5 is obtained over the whole BiSe thickness range of 3−16 nm. The hybridization of the topological surface state reduces the SCC signal when a TI is thinner than 6 nm,[33] but the maximum signal is at 3 nm, as shown in Figure 2e. The activation of the topological surface state or the suppression of bulk conduction at cryogenic temperature reduces the resistivity,[34,35] which is not observed in this work, as shown in Figure 1f. From all these facts, it is reasonable to consider sputtered polycrystalline BiSe as a normal conductor rather than a TI.

On the other hand, the cross-junction resistance (R_{CJ}) as a function of the thickness of BiSe as shown in Figure 3a,b disagrees with such a high resistivity of BiSe. The sketch in Figure 3a shows the measurement configuration of R_{CJ}. In the BiSe/Ti structures shown in Figure 3a, R_{CJ} shows a constant increase with the BiSe thickness from 2 to 16 nm, but the overall values are unexpectedly low. Even in BiSe/Pt devices shown in Figure 3b, although the change of R_{CJ} is higher than that of BiSe/Ti, the values are rather similar. This measurement assumes a vertical current flowing uniformly across the junction. Considering the large resistivity difference between BiSe and metallic wires such as Pt, Ti, and CoFe, the current stays in the CoFe until reaching the junction and flows vertically through BiSe to NM, so that the R_{CJ} is expected to be more than 80 Ω for 3-nm-thick BiSe when a resistivity of 18000 $\mu\Omega$ cm and a junction area of 80 nm × 80 nm are considered. However, the measured R_{CJ} on the devices with BiSe thicknesses up to 4 nm has negative values, which is generally considered as a transparent interface, hinting that the resistivity of BiSe may be lower than that initially measured in nanostructures without the NM. In order to reliably extract the resistivity of BiSe, we perform a 3D FEM simulation[36] of the R_{CJ} measurements, where the independently measured resistivities of the NM (Ti or Pt) and CoFe are used as inputs and the only unknown parameter is the BiSe resistivity. The 3D FEM simulation results are shown by red lines in Figure 3a,b. The resistivities of BiSe are calculated to be 600 $\mu\Omega$ cm for the BiSe/Ti structure, which is 30 times smaller than the values measured in the BiSe wire in Figure 1d, and 3700 $\mu\Omega$ cm in the BiSe/Pt structure, about 6 times higher than that of BiSe/Ti. These results indicate that the top NM layer changes the resistivity of BiSe. In the following paragraphs, we will discuss the origin of such a variation and the consequences in the quantification of the spin Hall effect in sputtered BiSe.

To understand the relationship between BiSe resistivity and the NM used, we performed TEM and EDX experiments in SiO_2 substrate/CoFe (15 nm)/BiSe (30 nm)/Ti (10 nm)/Pt (10 nm) and SiO_2 substrate/CoFe (15 nm)/BiSe (30 nm)/Pt (10 nm) multilayer stacks as shown in Figure 3c,d (see also Note S5 in the Supporting Information for the analysis of the actual BiSe/Ti local spin injection device). In order to obtain a quantitative elemental analysis from the EDX, we exfoliated single-crystal Bi_2Se_3 flakes on top of each stack. Since the Bi_2Se_3 flakes are stoichiometric, the composition of sputtered BiSe can be accurately determined by normalizing the Bi and Se intensity curves to 40% and 60%, respectively. In the BiSe/

https://doi.org/10.1021/acs.nanolett.2c03429
Nano Lett. 2022, 22, 7992−7999

Ti structure, a clear peak of the Se curve, indicated by the red arrow in Figure 3c, appears as a result of strong intermixing near Ti,[22−25] and BiSe has a 50:50 composition in the rest of the layer. No intermixing was observed between BiSe and Pt, where the composition was 45:55. Eventually, we obtained two different BiSe compositions depending on the chosen NM, even with the same growth condition. This is the reason the resistivity of BiSe varied from 600 to 3700 $\mu\Omega$ cm in the two structures depending on the NM used. The critical role of intermixing in SCC is further confirmed with harmonic Hall measurements (Note S6 in the Supporting Information).

Still, the composition change alone cannot explain the high resistivity (18000 $\mu\Omega$ cm) obtained in the BiSe wire measured laterally (Figure 1f). Using impedance measurements, we confirmed that there are two resistance elements, the grain and grain boundary (Note S7 in the Supporting Information). Accordingly, the absence of grain boundaries in the vertical direction for a BiSe thickness below 16 nm drastically reduces the BiSe resistivity when it is measured along this direction as compared to the lateral measurement, which includes the grain boundary contribution making a high noise level. The BiSe wire has a resistivity of 18000 $\mu\Omega$ cm as a series resistance of grain and grain boundary without intermixing, and the resistivity of 3700 $\mu\Omega$ cm measured vertically in the BiSe/Pt structure is of the parallel resistance of grain and grain boundary without intermixing. On the other hand, in the BiSe/Ti structure, the resistivity of 600 $\mu\Omega$ cm appears as a parallel resistance of grain and grain boundary accompanied by composition change due to intermixing. The different conditions are summarized in Table 1.

Table 1. Summary of BiSe Resistivities Depending on Measurement Direction and NM

structure	measurement direction	resistance of grain and boundary	intermixing	resistivity ($\mu\Omega$ cm)
BiSe wire	lateral	in series	no	18000
BiSe/Pt	vertical	in parallel	no (Se 55%)	3700
BiSe/Ti	vertical	in parallel	yes (Se 50%)	600

Returning to the SCC results of Figure 2e,f, it is necessary to accurately estimate θ_{SH} once again, because the resistivity of BiSe can affect the spin injection efficiency and current shunting, and consequently θ_{SH}. As a result of the 3D FEM simulation performed using the resistivity obtained in Figure 3a,b, a λ_s value of 0.5 nm and θ_{SH} value of 0.45 are estimated for the BiSe/Ti devices. In the case of BiSe/Pt devices, we extract a λ_s value of 0.35 nm and θ_{SH} value of 3.2. These results are significantly different from previously reported values[21,37] and our first estimation, because the high BiSe resistivity reduces the SCC signal by strong spin back flow. In addition, the SCC signal reduction as BiSe gets thicker is completely explained by the spin diffusion model for the entire thickness ranges, indicating the absence of quantum confinement depending on the grain size.[21]

By comparing our results with the reported results shown in Table 2, it is possible to strictly judge the SCC efficiency of sputtered BiSe. The BiSe thickness range used in this research covers all references in Table 2. The resistivity obtained in papers differs up to 1000 times[37,38] because of different growth conditions and measurement techniques. Only ref 38 reports a resistivity similar to that of the BiSe/Ti structure with also a similar θ_{SH}, in agreement with our claim. To compare with the results of spin pumping experiments, in which λ_{IREE} is used to quantify the SCC efficiency, the product $\lambda_s \cdot \theta_{SH}$ that is more relevant to the SCC efficiency in a local spin injection device is considered.[7,28,39] In particular, the θ_{SH} value of 18.62[21] is more than 50 times higher than 0.35 which is obtained in the BiSe/Ti structure, but the λ_{IREE} values of 0.32 nm[40] and 0.1 nm[41] are comparable to what we obtain in our local spin injection devices using BiSe/Ti (0.225 nm) despite differences in experimental methods and ferromagnetic materials. These results indicate that intermixing must be considered in material characterization, especially an appropriate resistivity quantification, and that θ_{SH} can be overestimated when these aspects are not properly considered.

To conclude, we observed all electrical spin-to-charge conversion in sputtered Bi_xSe_{1-x} in local spin injection devices at room temperature and showed that all parameters related to SCC efficiency, which are resistivity, λ_s, and θ_{SH}, were affected by intermixing with the adjacent nonmagnetic metal used to electrically shunt Bi_xSe_{1-x}. In particular, the fact that an Se concentration change by intermixing made a difference of 6 times in resistivity shows how easily θ_{SH} can be overestimated by resistivity without considering intermixing. Even though the SCC signal obtained in this study is too small to realize a MESO logic device, it allowed us to quantify the SCC efficiency of sputtered Bi_xSe_{1-x} in functional spintronic devices (instead of the commonly used Bi_xSe_{1-x}/FM bilayers). The potential of highly resistive sputtered Bi_xSe_{1-x} as the active element in the reading module can be exploited by improving different aspects, such as reducing the electrical noise caused by the grain boundary so that the top NM layer shunting the signal can be removed. The NM layer was applied to reduce the noise level in electrical measurements, but it is not a fundamental solution due to its low resistivity, leading to an overall SCC signal reduction. We suggest that the SCC efficiency and the SCC signal magnitude can be increased by protecting Bi_xSe_{1-x} with a tunneling barrier, such as MgO, to

Table 2. Summary of Spin-Related Parameters in This Work and Previous Reports

	BiSe thickness (nm)	ρ_{BiSe} ($\mu\Omega$ cm)	λ_s (nm)	θ_{SH}	λ_{IREE} (nm)	method	FM
$Bi_{50}Se_{50}$/Ti (this work)	2−16	600	0.5	0.45	0.225[a]	electrical spin injection	CoFe
$Bi_{45}Se_{55}$/Pt (this work)	3−5	3700	0.35	3.2	1.12[a]	electrical spin injection	CoFe
ref 21	4−40	12820		18.62[b]		harmonic Hall (dc)	CoFeB
ref 40	2−16				0.32[b]	spin pumping	CoFeB
ref 41	4−16				0.11[b]	spin pumping	YIG
ref 37	5−10	1000000		75		ST-FMR[c]	Py
ref 38.	3−15	890		0.35		harmonic Hall (ac)	Co

[a] $\lambda_{IREE} = \theta_{SH} \cdot \lambda_s$. [b] The maximum value of the thickness dependence is indicated. [c] Spin torque-ferromagnetic resonance.

https://doi.org/10.1021/acs.nanolett.2c03429
Nano Lett. 2022, 22, 7992−7999

prevent intermixing, current shunting, and spin back flow, while enhancing the spin injection efficiency.

METHODS

Device Nanofabrication. The devices were fabricated on Si/SiO_2 substrates by e-beam lithography, sputter deposition, ion-milling and lift-off processes. The CoFe wire is patterned as the first layer and deposited by dc magnetron sputtering of 30 W at 2 mTorr of Ar pressure. To eliminate a sidewall of CoFe, ion-milling (Ar flow of 15 sccm, acceleration voltage of 50 V, beam current of 50 mA, and beam voltage of 300 V) is performed with an incident beam angle of 80° after the lift-off process. The T-shaped wire is patterned as the second layer and BiSe is deposited by magnetron sputtering of the Bi_2Se_3 target using an rf power of 35 W at 3 mTorr. Subsequently, NM is deposited *in situ* using dc power (80 W for Pt, 100 W for Ti, 200 W for Ta) at 3 mTorr.

Materials Characterization. TEM, STEM, and EDX data were obtained on a Titan G2 60-300 (FEI, The Netherlands) (scanning) transmission electron microscope at 300 kV accelerating voltage. The microscope was equipped with a high brightness xFEG, an imaging Cs corrector, a STEM HAADF detector, and an EDX RTEM spectrometer (EDAX, UK). Cross-sectional TEM samples of the devices and multilayers were prepared by a standard FIB technique.

Electrical Measurements. Electronic transport measurements were performed with a Physical Property Measurement System (PPMS) from Quantum Design, using a "dc reversal" technique with a Keithley 2182 nanovoltmeter and a 6221 current source. The second harmonic Hall measurements are performed with a PPMS using an ac Transport Measurement System. A magnetic field is applied by a superconducting solenoid magnet, and a rotatable sample stage is used.

ASSOCIATED CONTENT

Supporting Information

The Supporting Information is available free of charge at https://pubs.acs.org/doi/10.1021/acs.nanolett.2c03429.

> Further information about TEM and EDX characterization of additional stacks, spin-to-charge conversion in Ta local spin injection device, quantification of spurious effects (AHE from CoFe and OHE from Pt), spin diffusion 3D FEM simulation for spin-to-charge conversion, impedance measurements, and second harmonic Hall measurement of spin torque (PDF)

AUTHOR INFORMATION

Corresponding Authors

Won Young Choi − *CIC nanoGUNE BRTA, 20018 Donostia-San Sebastián, Basque Country, Spain;* orcid.org/0000-0001-8839-5665; Email: w.choi@nanogune.eu

Fèlix Casanova − *CIC nanoGUNE BRTA, 20018 Donostia-San Sebastián, Basque Country, Spain; IKERBASQUE, Basque Foundation for Science, 48009 Bilbao, Basque Country, Spain;* orcid.org/0000-0003-0316-2163; Email: f.casanova@nanogune.eu

Authors

Isabel C. Arango − *CIC nanoGUNE BRTA, 20018 Donostia-San Sebastián, Basque Country, Spain*

Van Tuong Pham − *Univ. Grenoble Alpes, CNRS, Institut Neel, F-38000 Grenoble, France*

Diogo C. Vaz − *CIC nanoGUNE BRTA, 20018 Donostia-San Sebastián, Basque Country, Spain;* orcid.org/0000-0001-8490-2818

Haozhe Yang − *CIC nanoGUNE BRTA, 20018 Donostia-San Sebastián, Basque Country, Spain*

Inge Groen − *CIC nanoGUNE BRTA, 20018 Donostia-San Sebastián, Basque Country, Spain*

Chia-Ching Lin − *Components Research, Intel Corp., Hillsboro, Oregon 97124, United States*

Emily S. Kabir − *Components Research, Intel Corp., Hillsboro, Oregon 97124, United States*

Kaan Oguz − *Components Research, Intel Corp., Hillsboro, Oregon 97124, United States*

Punyashloka Debashis − *Components Research, Intel Corp., Hillsboro, Oregon 97124, United States*

John J. Plombon − *Components Research, Intel Corp., Hillsboro, Oregon 97124, United States*

Hai Li − *Components Research, Intel Corp., Hillsboro, Oregon 97124, United States;* orcid.org/0000-0001-7668-569X

Dmitri E. Nikonov − *Components Research, Intel Corp., Hillsboro, Oregon 97124, United States*

Andrey Chuvilin − *CIC nanoGUNE BRTA, 20018 Donostia-San Sebastián, Basque Country, Spain; IKERBASQUE, Basque Foundation for Science, 48009 Bilbao, Basque Country, Spain*

Luis E. Hueso − *CIC nanoGUNE BRTA, 20018 Donostia-San Sebastián, Basque Country, Spain; IKERBASQUE, Basque Foundation for Science, 48009 Bilbao, Basque Country, Spain;* orcid.org/0000-0002-7918-8047

Ian A. Young − *Components Research, Intel Corp., Hillsboro, Oregon 97124, United States*

Complete contact information is available at: https://pubs.acs.org/10.1021/acs.nanolett.2c03429

Author Contributions

W.Y.C. and I.C.A. contributed equally.

Notes

The authors declare no competing financial interest.

ACKNOWLEDGMENTS

We acknowledge C. Rufo, R. Llopis, and R. Gay for technical assistance with the sample fabrication. This work was supported by Intel Corporation through the Semiconductor Research Corporation under MSR-INTEL TASK 2017-IN-2744 and the "FEINMAN" Intel Science Technology Center and by the Spanish MICINN under Project No. RTI2018-094861-B-I00 and under the Maria de Maeztu Units of Excellence Programme (MDM-2016-0618 and CEX2020-001038-M). W.Y.C. acknowledges postdoctoral fellowship support from the "Juan de la Cierva Formación" programme by the Spanish MICINN (Grant No. FJC2018-038580-I). D.C.V. acknowledges support from the European Commission for a Marie Sklodowska-Curie individual fellowship (Grant No. 892983-SPECTER).

REFERENCES

(1) Moore, G. E. Cramming more components onto integrated circuits. *Proc. IEEE* **1998**, *86*, 82−85.

(2) Gelsinger, P. P. Microprocessors for the new millennium: Challenges opportunities and new frontiers. *IEEE Int. Solid-State Circuits Conf. (ISSCC) Dig. Technol. Papers* **2001**, 22−25.
(3) Horowitz, M. Computing's energy problem (and what we can do about it). *IEEE Int. Solid-State Circuits Conf. (ISSCC) Dig. Technol. Papers* **2014**, 10−14.
(4) Manipatruni, S.; Nikonov, D. E.; Young, I. A. Beyond CMOS computing with spin and polarization. *Nat. Phys.* **2018**, *14*, 338−343.
(5) Manipatruni, S.; Nikonov, D. E.; Lin, C.-C.; Gosavi, T. A.; Liu, H.; Prasad, B.; Huang, Y.-L.; Bonturim, E.; Ramesh, R.; Young, I. A. Scalable energy-efficient magnetoelectric spin−orbit logic. *Nature* **2019**, *565*, 35−42.
(6) Li, H.; Lin, C.-C.; Nikonov, D. E.; Young, I. A. Differential Electrically Insulated Magnetoelectric Spin-Orbit Logic Circuits. *IEEE J. Explor. Solid-State Comput. Devices Circuits* **2021**, *7*, 18−25.
(7) Pham, V. T.; Groen, I.; Manipatruni, S.; Choi, W. Y.; Nikonov, D. E.; Sagasta, E.; Lin, C.-C.; Gosavi, T. A.; Marty, A.; Hueso, L. E.; Young, I. A.; Casanova, F. Spin−orbit magnetic state readout in scaled ferromagnetic/heavy metal nanostructures. *Nat. Electron.* **2020**, *3*, 309−315.
(8) Manchon, A.; Koo, H. C.; Nitta, J.; Frolov, S. M.; Duine, R. A. New perspectives for Rashba spin−orbit coupling. *Nat. Mater.* **2015**, *14*, 871−882.
(9) Gilbert, M. J. Topological electronics. *Commun. Phys.* **2021**, *4*, 70.
(10) Zhang, S.; Fert, A. Conversion between spin and charge currents with topological insulators. *Phys. Rev. B* **2016**, *94*, 184423.
(11) Mellnik, A. R.; Lee, J. S.; Richardella, A.; Grab, J. L.; Mintun, P. J.; Fischer, M. H.; Vaezi, A.; Manchon, A.; Kim, E.-A.; Samarth, N.; Ralph, D. C. Spin-transfer torque generated by a topological insulator. *Nature* **2014**, *511*, 449−451.
(12) Fan, Y.; Upadhyaya, P.; Kou, X.; Lang, M.; Takei, S.; Wang, Z.; Tang, J.; He, L.; Chang, L.-T.; Montazeri, M.; Yu, G.; Jiang, W.; Nie, T.; Schwartz, R. N.; Tserkovnyak, Y.; Wang, K. L. Magnetization switching through giant spin−orbit torque in a magnetically doped topological insulator heterostructure. *Nat. Mater.* **2014**, *13*, 699−704.
(13) Han, J.; Richardella, A.; Siddiqui, S. A.; Finley, J.; Samarth, N.; Liu, L. Room-Temperature Spin-Orbit Torque Switching Induced by a Topological Insulator. *Phys. Rev. Lett.* **2017**, *119*, 077702.
(14) Khang, N. H. D.; Ueda, Y.; Hai, P. N. A conductive topological insulator with large spin Hall effect for ultralow power spin−orbit torque switching. *Nat. Mater.* **2018**, *17*, 808−813.
(15) Shao, Q.; Wu, H.; Pan, Q.; Zhang, P.; Pan, L.; Wong, K.; Che, X.; Wang, K. L. Room Temperature Highly Efficient Topological Insulator/Mo/CoFeB Spin-Orbit Torque Memory with Perpendicular Magnetic Anisotropy. *2018 IEEE Int. Elec. Dev. Meeting (IEDM)* **2018**, 36.3.1−36.3.4.
(16) Khokhriakov, D.; Hoque, A. Md; Karpiak, B.; Dash, S. P. Gate-tunable spin-galvanic effect in graphene-topological insulator van der Waals heterostructures at room temperature. *Nat. Commun.* **2020**, *11*, 3657.
(17) Barua, S.; Rajeev, K. P. Status of surface conduction in topological insulators. *AIP Advances* **2014**, *4*, 017135.
(18) Wu, H.; Zhang, P.; Deng, P.; Lan, Q.; Pan, Q.; Razavi, S. A.; Che, X.; Huang, L.; Dai, B.; Wong, K.; Han, X.; Wang, K. L. Room-Temperature Spin-Orbit Torque from Topological Surface States. *Phys. Rev. Lett.* **2019**, *123*, 207205.
(19) Liu, L.; Richardella, A.; Garate, I.; Zhu, Y.; Samarth, N.; Chen, C.-T. Spin-polarized tunneling study of spin-momentum locking in topological insulators. *Phys. Rev. B* **2015**, *91*, 235437.
(20) Li, C. H.; van 't Erve, O. M. J.; Yan, C.; Li, L.; Jonker, B. T. Electrical Detection of Charge-to-spin and Spin-to-Charge Conversion in a Topological Insulator Bi_2Te_3 Using BN/Al_2O_3 Hybrid Tunnel Barrier. *Sci. Rep.* **2018**, *8*, 10265.
(21) DC, M.; Grassi, R.; Chen, J.-Y.; Jamali, M.; Hickey, D. R.; Zhang, D.; Zhao, Z.; Li, H.; Quarterman, P.; Lv, Y.; Li, M.; Manchon, A.; Mkhoyan, K. A.; Low, T.; Wang, J.-P. Room-temperature high spin−orbit torque due to quantum confinement in sputtered $Bi_xSe_{(1-x)}$ films. *Nat. Mater.* **2018**, *17*, 800−807.
(22) Walsh, L. A.; Smyth, C. M.; Barton, A. T.; Wang, Q.; Che, Z.; Yue, R.; Kim, J.; Kim, M. J.; Wallace, R. M.; Hinkle, C. L. Interface Chemistry of Contact Metals and Ferromagnets on the Topological Insulator Bi_2Se_3. *J. Phys. Chem. C* **2017**, *121* (42), 23551−23563.
(23) Ferfolja, K.; Valant, M.; Mikulska, I.; Gardonio, S.; Fanetti, M. Chemical Instability of an Interface between Silver and Bi_2Se_3 Topological Insulator at Room Temperature. *J. Phys. Chem. C* **2018**, *122* (18), 9980−9984.
(24) Ferfolja, K.; Fanetti, M.; Gardonio, S.; Panighel, M.; Píš, I.; Nappini, S.; Valant, M. A cryogenic solid-state reaction at the interface between Ti and the Bi_2Se_3 topological insulator. *J. Mater. Chem. C* **2020**, *8*, 11492−11498.
(25) Bonell, F.; Goto, M.; Sauthier, G.; Sierra, J. F.; Figueroa, A. I.; Costache, M. V.; Miwa, S.; Suzuki, Y.; Valenzuela, S. O. Control of Spin−Orbit Torques by Interface Engineering in Topological Insulator Heterostructures. *Nano Lett.* **2020**, *20*, 5893−5899.
(26) Du, C.; Wang, H.; Yang, F.; Hammel, P. C. Systematic variation of spin-orbit coupling with d-orbital filling: Large inverse spin Hall effect in 3d transition metals. *Phys. Rev. B* **2014**, *90*, 140407.
(27) Wang, H. L.; Du, C. H.; Pu, Y.; Adur, R.; Hammel, P. C.; Yang, F. Y. Scaling of Spin Hall Angle in 3d, 4d, and 5d Metals from $Y_3Fe_5O_{12}$/Metal Spin Pumping. *Phys. Rev. Lett.* **2014**, *112*, 197201.
(28) Sagasta, E.; Omori, Y.; Isasa, M.; Gradhand, M.; Hueso, L. E.; Niimi, Y.; Otani, Y.; Casanova, F. Tuning the spin Hall effect of Pt from the moderately dirty to the superclean regime. *Phys. Rev. B* **2016**, *94*, 060412.
(29) Pham, V. T.; Vila, L.; Zahnd, G.; Marty, A.; Savero-Torres, W.; Jamet, M.; Attané, J.-P. Ferromagnetic/nonmagnetic nanostructures for the electrical measurement of the spin Hall effect. *Nano Lett.* **2016**, *16*, 6755−6760.
(30) Groen, I.; Pham, V. T.; Leo, N.; Marty, A.; Hueso, L. E.; Casanova, F. Disentangling Spin, Anomalous, and Planar Hall Effects in Ferromagnet−Heavy-Metal Nanostructures. *Phys. Rev. Applied* **2021**, *15*, 044010.
(31) Safeer, C. K.; Herling, F.; Choi, W. Y.; Ontoso, N.; Ingla-Aynés, J.; Hueso, L. E.; Casanova, F. Reliability of spin-to-charge conversion measurements in graphene-based lateral spin valves. *2D Mater.* **2022**, *9*, 015024.
(32) Pham, V. T.; Zahnd, G.; Marty, A.; Savero Torres, W.; Jamet, M.; Noël, P.; Vila, L.; Attané, J. P. Electrical detection of magnetic domain walls by inverse and direct spin Hall effect. *Appl. Phys. Lett.* **2016**, *109*, 192401.
(33) Linder, J.; Yokoyama, T.; Sudbø, A. Anomalous finite size effects on surface states in the topological insulator Bi_2Se_3. *Phys. Rev. B* **2009**, *80*, 205401.
(34) Dankert, A.; Geurs, J.; Kamalakar, M. V.; Charpentier, S.; Dash, S. P. Room Temperature Electrical Detection of Spin Polarized Currents in Topological Insulators. *Nano Lett.* **2015**, *15*, 7976−7981.
(35) Dankert, A.; Bhaskar, P.; Khokhriakov, D.; Rodrigues, I. H.; Karpiak, B.; Kamalakar, M. V.; Charpentier, S.; Garate, I.; Dash, S. P. Origin and evolution of surface spin current in topological insulators. *Phys. Rev. B* **2018**, *97*, 125414.
(36) Pham, V. T.; Cosset-Chéneau, M.; Brenac, A.; Boulle, O.; Marty, A.; Attané, J.-P.; Vila, L. Evidence of interfacial asymmetric spin scattering at ferromagnet-Pt interfaces. *Phys. Rev. B* **2021**, *103*, L201403.
(37) Ramaswamy, R.; Dutta, T.; Liang, S.; Yang, G.; Saifullah, M. S. M.; Yang, H. Spin orbit torque driven magnetization switching with sputtered Bi_2Se_3 spin current source. *J. Phys. D: Appl. Phys.* **2019**, *52*, 224001.
(38) Zhang, X.; Cui, B.; Mao, J.; Yun, J.; Yan, Z.; Chang, M.; Zuo, Y.; Xi, L. Topological Surface States-Induced Perpendicular Magnetization Switching in $Pt/Co/Bi_2Se_3$ Heterostructures. *Phys. Status Solidi RRL* **2020**, *14*, 2000033.
(39) Rojas-Sánchez, J.-C.; Fert, A. Compared Efficiencies of Conversions between Charge and Spin Current by Spin-Orbit Interactions in Two- and Three-Dimensional Systems. *Phys. Rev. Applied* **2019**, *11*, 054049.

https://doi.org/10.1021/acs.nanolett.2c03429
Nano Lett. 2022, 22, 7992−7999

(40) DC, M.; Chen, J.-Y.; Peterson, T.; Sahu, P.; Ma, B.; Mousavi, N.; Harjani, R.; Wang, J.-P. Observation of High Spin-to-Charge Conversion by Sputtered Bismuth Selenide Thin Films at Room Temperature. *Nano Lett.* **2019**, *19* (8), 4836−4844.
(41) DC, M.; Liu, T.; Chen, J.-Y.; Peterson, T.; Sahu, P.; Li, H.; Zhao, Z.; Wu, M.; Wang, J.-P. Room-temperature spin-to-charge conversion in sputtered bismuth selenide thin films via spin pumping from yttrium iron garnet. *Appl. Phys. Lett.* **2019**, *114*, 102401.

https://doi.org/10.1021/acs.nanolett.2c03429
Nano Lett. 2022, 22, 7992−7999